Joule

CellPress

Article

Stabilizing the α-Phase of $CsPbI_3$ Perovskite by Sulfobetaine Zwitterions in One-Step Spin-Coating Films

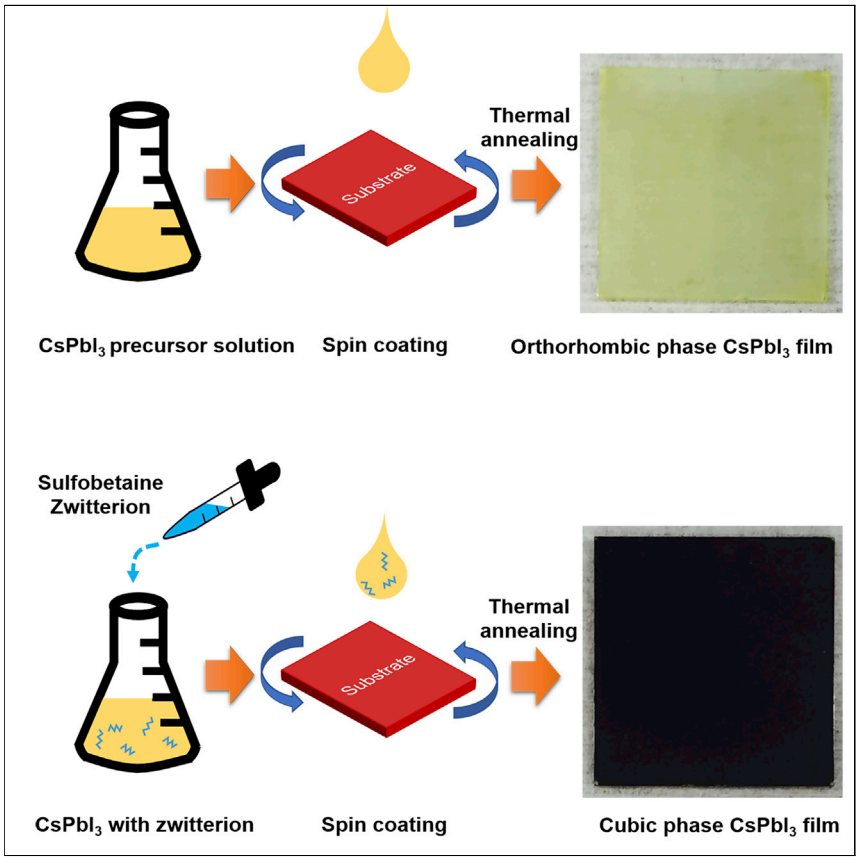

Stabilizing the α phase of $CsPbI_3$ has become one of the most critical prerequisites for its photovoltaic application. We found that mixing a small amount of sulfobetaine zwitterions in $CsPbI_3$ precursor solution could stabilize the α phase of $CsPbI_3$ films at room temperature. The interaction of zwitterion with $CsPbI_3$ impeded the fast crystallization of $CsPbI_3$, which reduced $CsPbI_3$ grain size to stabilize the α phase. Solar cells with these α-phase $CsPbI_3$ films showed stabilized efficiency of 11.4% under 1-sun illumination.

Qi Wang, Xiaopeng Zheng, Yehao Deng, Jingjing Zhao, Zhaolai Chen, Jinsong Huang

jhuang@unc.edu

HIGHLIGHTS

Three sulfobetaine zwitterions were used to stabilize the α phase of $CsPbI_3$ films

The zwitterions could impede $CsPbI_3$ crystallization to form small-grained films

The increased grain surface energy stabilized the α phase of $CsPbI_3$ films

Solar cells with these $CsPbI_3$ films showed PCE of 11.4% under 1-sun illumination

Wang et al., Joule 1, 371–382
October 11, 2017
http://dx.doi.org/10.1016/j.joule.2017.07.017

Joule

CellPress

Article

Stabilizing the α-Phase of $CsPbI_3$ Perovskite by Sulfobetaine Zwitterions in One-Step Spin-Coating Films

Qi Wang,[1] Xiaopeng Zheng,[1] Yehao Deng,[1] Jingjing Zhao,[1] Zhaolai Chen,[1] and Jinsong Huang[1,2,3,*]

SUMMARY

Inorganic cesium lead halide perovskites ($CsPbI_3$) are promising materials for efficient wide-bandgap perovskite solar cells, but they suffer from a phase transition from black α phase to yellow δ phase at room temperature. Here, we report a facile method to stabilize the α-phase $CsPbI_3$ films via a single-step film deposition process. A small amount (~1.5 wt %) of sulfobetaine zwitterion mixed in $CsPbI_3$ precursor solution could facilitate the formation of black-phase $CsPbI_3$ films that show significantly improved phase stability in air. The black-phase stabilization can be explained by the formation of small $CsPbI_3$ grains with average size of ~30 nm, which increased the grain surface area to stabilizes the α phase. The zwitterions were found to impede the crystallization of $CsPbI_3$ perovskite films via electrostatic interaction with the ions and colloids in the $CsPbI_3$ precursor solution. Solar cells using these zwitterion-stabilized perovskite films showed stabilized power conversion efficiency of 11.4% under 1-sun illumination.

INTRODUCTION

The emergence of organic-inorganic halide perovskite (OIHP) solar cells has generated enormous research interest in the photovoltaic community.[1–14] Blessed with the excellent optoelectronic properties of OIHP materials, the power conversion efficiency (PCE) of OIHP solar cells has skyrocketed from ~3% to certified ~22% in several years.[15] Despite the excellent performance, the volatile organic cations in OIHP materials, such as methylammonium (MA) and formamidinium (FA), have raised concerns about the stability of perovskite materials to external stimuli, particularly heat and light.[16] Thermal-induced decomposition of methylammonium lead halide perovskite ($MAPbI_3$) films at temperature above 85°C has been reported.[16,17] Alternatively, perovskites with inorganic cations, such as $CsPbI_3$, have recently gained increasing attention, because $CsPbI_3$ is stable up to their melting points above 460°C.[18] $CsPbI_3$ in cubic crystal structure (α phase) has a bandgap of 1.73 eV,[19] which is suitable for photovoltaic application and especially attractive as the top cells for perovskite/silicon tandem solar cells. However, $CsPbI_3$ could quickly transit to yellow phase (δ phase) at temperatures below 315°C, which basically does not absorb much sun light.[20,21] To address this problem, one general method reported in the literature involves partially substituting iodide with bromide to tune the tolerance factor of the perovskite structure.[19,22,23] However, the ratio of bromide in $CsPb(Br_xI_{1-x})_3$ usually needs to be larger than 33% to stabilize the cubic phase,[19,22,23] which undesirably increases the perovskite bandgap to 1.9 eV and causes the loss of absorption in the red-light region. Recently, thermally evaporated $CsPbI_3$ films were reported to maintain the α phase at room temperature.[22,24] But its

Context & Scale

Due to the superior photovoltaic performance and enormous potential for commercialization, perovskite materials have attracted much attention in the past years. Particularly, $CsPbI_3$ is a cutting-edge material for efficient wide-bandgap solar cells that can potentially boost the efficiency of silicon solar cells with tandem structure. However, $CsPbI_3$ material suffers from a notorious phase transition from black α phase to yellow δ phase at room temperature, which dramatically reduces the absorbed sun light to reduce photovoltaic performance. Here, sulfobetaine zwitterions were mixed in $CsPbI_3$ precursor solution to stabilize the α phase of $CsPbI_3$ films. Solar cells with these α-$CsPbI_3$ films exhibited excellent performance and stability. The α-phase $CsPbI_3$ films may also be used to fabricate efficient light-emitting diodes or photodetectors. The method of phase manipulation may be used in stabilizing the black phase of other perovskite photovoltaic materials, such as $FAPbI_3$ and $CsSnI_3$.

long-term phase stability still requires further verification, because there is no clear mechanism behind this kind of phase stabilization.

Another promising method to stabilize the α phase of $CsPbI_3$ involved tuning the free energy by forming $CsPbI_3$ quantum dots.[25] The thermodynamic stability of an individual phase is determined by the total Gibbs free energy with contributions from both the material surface and the bulk. Reducing material size could increase the surface/volume ratio, so that certain phases that are unstable in bulk material could be stabilized due to the dominant contribution of surface energy to the total Gibbs energy. One well-known example is the phase transition of aluminum oxide (Al_2O_3) from the rhombohedral structure (α phase) in bulky material to the cubic structure (γ phase) in nanoparticles, because the surface energy of γ-phase Al_2O_3 is much lower than that of the α phase.[26] The phenomenon of size-dependent phase transition has also been observed in many other materials, including perovskite materials such as $BaTiO_3$,[27] $PbTiO_3$,[28] and $La_{1-x}Sr_xMnO_3$.[29] Interestingly, one empirical rule summarized from many materials is that materials tend to convert to a more symmetric crystal structure when the dimensions reduce,[30] because symmetrical structures usually have smaller surface energy, which could also explain the stabilization of the cubic phase in $CsPbI_3$ quantum dots.[25] Solar cells with $CsPbI_3$ quantum dots showed high PCE of >10%.[25] However, the quantum dot cell fabrication process was complicated, including dedicated and lengthy quantum dot synthesis and multiple-cycle quantum dot coating and ligand washing. A simple and low-cost fabrication method for α-phase $CsPbI_3$ films is highly desired for the further development of these inorganic cesium perovskite solar cells.

In this article, we report a simple method to stabilize α-phase $CsPbI_3$ films via a single-step film deposition process. It was found that mixing a small amount of sulfobetaine zwitterion (~1.5 wt %) in $CsPbI_3$ precursor solution could stabilize the α phase of $CsPbI_3$ films at room temperature. The zwitterion molecules impede the fast crystallization of $CsPbI_3$ perovskite by interacting with ions and colloids in the $CsPbI_3$ precursor solution. Solar cells with these zwitterion-stabilized perovskite films showed stabilized efficiency of 11.4% under 1-sun illumination.

RESULTS AND DISCUSSION

Stabilization of α-Phase $CsPbI_3$ Films with Zwitterions

The $CsPbI_3$ films in this study were fabricated by a one-step spin-coating method, which has been widely used in fabricating highly efficient OIHP solar cells.[31–33] Certain ligands or additives were added to reduce the grain size of $CsPbI_3$ films to stabilize the cubic-phase $CsPbI_3$. We started our research with mixing the $CsPbI_3$ precursor solution with the ligands used in synthesizing $CsPbI_3$ quantum dots, such as oleylamine and oleic acid.[25,34,35] However, the spun $CsPbI_3$ films with these ligands still showed yellow color. Encouragingly, we discovered in the presence of sulfobetaine zwitterions, the spun $CsPbI_3$ films could quickly turn to black after annealing the film at ~80°C for several seconds. Details about the film fabrication method can be found in the Experimental Procedures. In short, we tried three sulfobetaine zwitterions, 3-(1-pyridinio)-1-propanesulfonate (NDSB201), 3-[2-hydroxyethyl(dimethyl)azaniumyl] propane-1-sulfonate (NDSB211), and 3-(decyldimethylammonio) propane-1-sulfonate (SB3-10). The molecular structures of these zwitterions are shown in Figure 1A. All of them could effectively stabilize the black phase of $CsPbI_3$ films. Figure 1B shows the absorption spectra of the $CsPbI_3$ films with or without NDSB201 zwitterion. The NDSB201-stabilized $CsPbI_3$ films have an absorption cut-off at ~720 nm, corresponding to an optical bandgap of 1.72 eV,

[1]Department of Mechanical and Materials Engineering, University of Nebraska-Lincoln, Lincoln, NE 68588, USA

[2]Department of Applied Physical Sciences, University of North Carolina, Chapel Hill, NC 27599, USA

[3]Lead Contact

*Correspondence: jhuang@unc.edu

http://dx.doi.org/10.1016/j.joule.2017.07.017

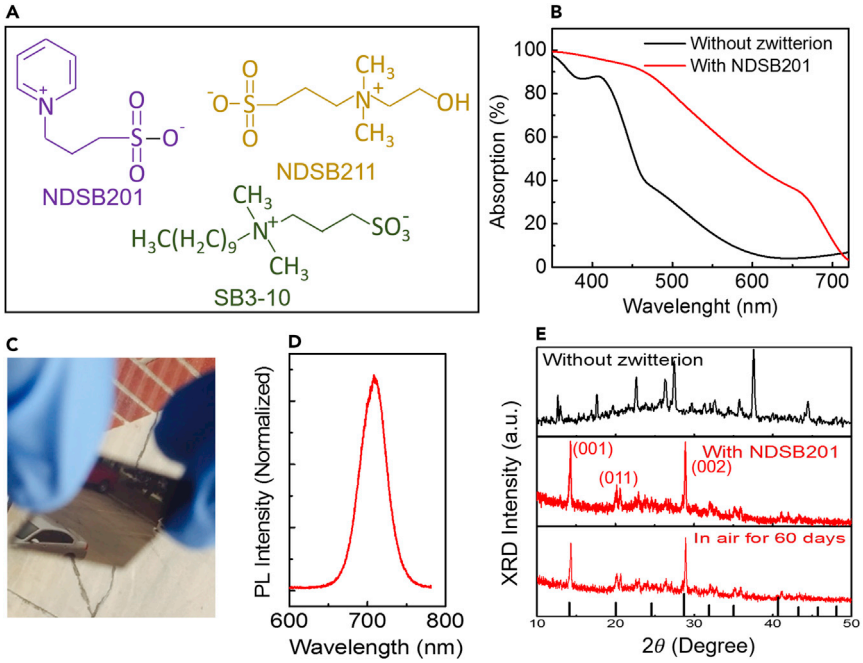

Figure 1. α-Phase $CsPbI_3$ Films Stabilized by Sulfobetaine Zwitterions

(A) Molecular structures of the sulfobetaine zwitterions used in this study.

(B) Absorption spectra of $CsPbI_3$ perovskite films with or without NDSB201 zwitterion.

(C) A $CsPbI_3$ perovskite film with zwitterion. The zwitterion-stabilized $CsPbI_3$ film has a black and mirror-like surface.

(D) PL spectrum of a $CsPbI_3$ perovskite film with zwitterion.

(E) XRD patterns of perovskite films without (top) and with (middle) NDSB201 zwitterion. The XRD pattern of zwitterion-stabilized $CsPbI_3$ film matches the simulated XRD pattern of α-phase $CsPbI_3$ (black lines at the bottom of the figures). The bottom XRD pattern shows no obvious phase change after the α-phase $CsPbI_3$ film was stored in air for 60 days.

while the absorption edge of the $CsPbI_3$ films without zwitterion is around 620 nm. Figure 1C shows that the SB3-10-stabilized $CsPbI_3$ film is black and has a mirror-like smooth surface. After annealing the sample overnight at 100°C, the film still maintained the black color as shown in Figure S1. In Figure 1D, the photoluminescence (PL) spectrum of the black-phase $CsPbI_3$ film exhibits a single emission peak at ~710 nm. X-ray diffraction (XRD) patterns of the $CsPbI_3$ films with or without NDSB201 zwitterion are shown in Figure 1E. The solid lines at the bottom of the figure represent the simulated XRD pattern of cubic-phase $CsPbI_3$. The main XRD peaks of the zwitterion-stabilized $CsPbI_3$ film located at 14.4°, 20.2°, and 28.8° could be indexed to the (001), (011), and (002) planes of α-phase $CsPbI_3$, respectively, although some small peaks were also detected that were probably from impurities. The zwitterion-stabilized films stayed in the black cubic phase after storage in air for 2 months (Figure 1E).

Mechanism of α-Phase Stabilization

We speculated that the added zwitterion molecules could impede $CsPbI_3$ crystallization to form small-grained $CsPbI_3$ films. To verify this, we compared the grain sizes of the $CsPbI_3$ films with or without SB3-10 zwitterion by cross-section scanning electron microscopy (SEM). As shown in Figure 2A, the $CsPbI_3$ film with the SB3-10 zwitterion contained many small grains with an average grain size of ~30 nm. In striking contrast, the $CsPbI_3$ film without zwitterion in Figure 2B shows a totally different morphology with much larger gain size, which verifies that the added zwitterions played a crucial role in reducing the grain size of $CsPbI_3$ films. The formation of much larger grains in the $CsPbI_3$ films without zwitterion may correlate with the

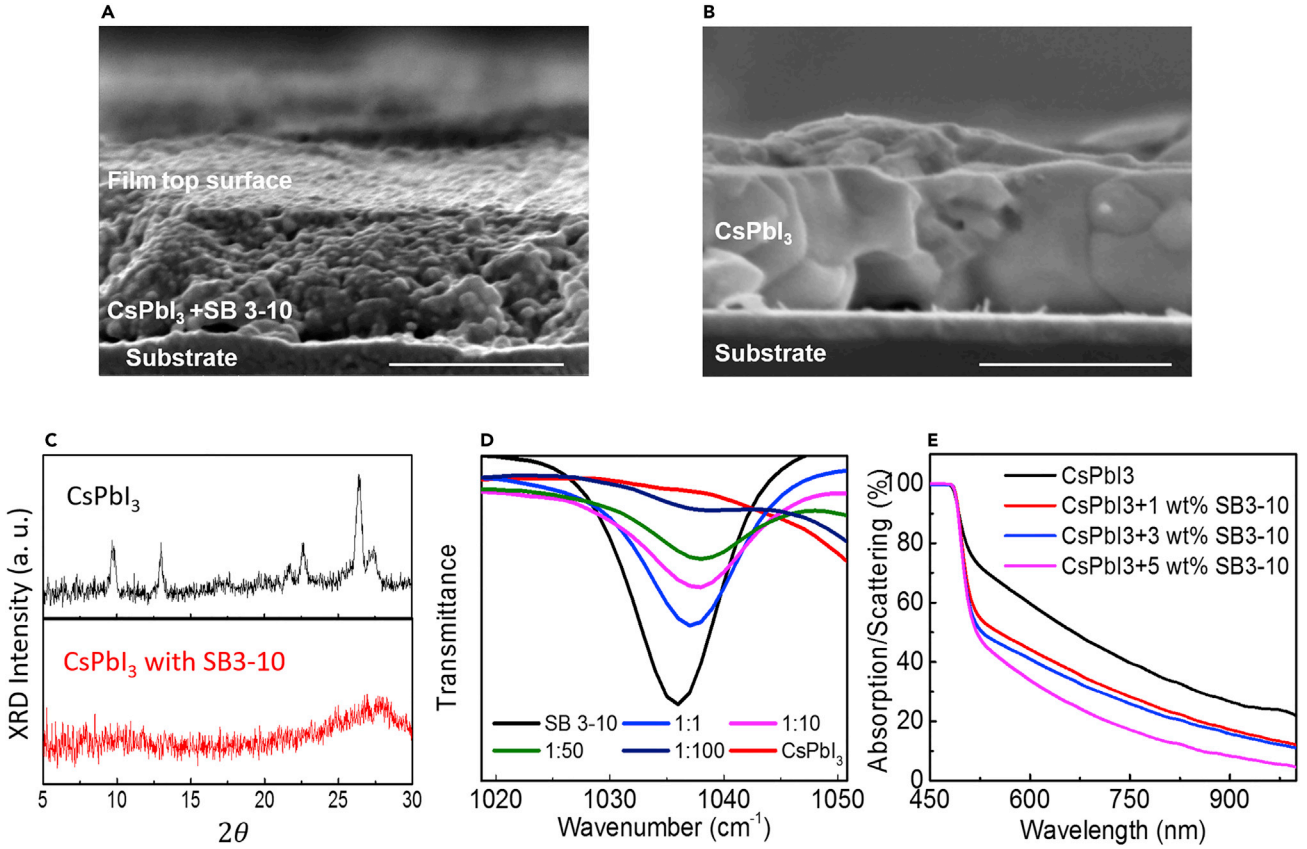

Figure 2. Characterizations to Identify the Origin of α-Phase Stabilization

(A and B) Cross-section SEM images of $CsPbI_3$ films with (A) or without (B) SB3-10 zwitterion. The scale bars of the images represent 400 nm.

(C) XRD patterns of the perovskite spun films fabricated by precursor solutions without (up) and with (bottom) SB3-10 zwitterion. No thermal annealing was applied on the films, and the spun films were measured immediately after fabrication.

(D) FTIR measurement of SB3-10 solution and SB3-10 solutions mixed with different ratios of $CsPbI_3$. The molar ratio of SB3-10 to $CsPbI_3$ varied from 1:1 to 1:100.

(E) UV-visible spectroscopy measurement of the $CsPbI_3$ solution and $CsPbI_3$ solutions mixed with different weight percentages of SB3-10.

fast crystallization of the $CsPbI_3$ films. To demonstrate that, we compared the XRD patterns of $CsPbI_3$ spun films fabricated by precursor solutions with or without SB3-10 zwitterion. Details about the sample preparation can be found in the Experimental Procedures. In short, no thermal annealing was applied on the spun films, and all the XRD patterns of the films were measured immediately after fabrication. As shown in Figure 2C, clear XRD peaks were observed in the spun $CsPbI_3$ film without zwitterion, which can be indexed as δ-phase $CsPbI_3$,[36] indicating quick crystallization of δ-phase $CsPbI_3$ at room temperature without thermal annealing. In striking contrast, the spun $CsPbI_3$ film with zwitterion was amorphous without any obvious XRD peak (Figure 2C). This demonstrates that the crystallization of $CsPbI_3$ perovskite was suppressed by the added SB3-10 zwitterion, which explains the formation of small grains in the zwitterion-stabilized $CsPbI_3$ films.

We examined two hypotheses that may explain the formation of the amorphous phase in the zwitterion-stabilized $CsPbI_3$ films: (1) steric effect of the zwitterion long ligands and (2) interaction of zwitterion with perovskite ions in the precursor solution. If the amorphous phase is caused by the long carbon chains of zwitterion molecules, we expect many other materials with long carbon chains could also suppress the crystallization of $CsPbI_3$ to form amorphous spun films. However, it turned

out that the zwitterions are unique in terms of forming amorphous phase films. We tested XRD patterns of the $CsPbI_3$ spun films fabricated by $CsPbI_3$ precursor solutions mixed with four other materials with long carbon chains: oleic acid, oleylamine, 1-octadecylamine, and polyvinyl alcohol. The XRD patterns in Figure S2 show that all these spun films without thermal annealing exhibit obvious δ-phase $CsPbI_3$ peaks. All these films showed yellow color after thermal annealing at 100°C for 20 min. The cross-section SEM images in Figure S3 show the morphologies of these annealed $CsPbI_3$ films, where none of the added material could form small-grained $CsPbI_3$ film. It is interesting to find that the sulfobetaine zwitterions are unique in suppressing $CsPbI_3$ crystallization to form small-grained films, implying the functional groups in sulfobetaine zwitterions, a quaternary amine (N^+) group and a sulfonate group (SO_3^-), may play a crucial role in the formation of the amorphous phase and small-grained films.

Several experiments were conducted to verify the interaction of the sulfobetaine zwitterions with ions in the precursor solution. We first conducted Fourier transform infrared spectroscopy (FTIR) measurements to confirm the interaction of sulfobetaine zwitterions with Cs^+ and Pb^{2+} cations in the precursor solution. Figure 2D shows the FTIR spectra of $CsPbI_3$ solution, SB3-10 zwitterion solution, and $CsPbI_3$-zwitterion mixed solutions. The FTIR peaks located around 1,035 cm^{-1} represent the symmetric S=O stretches of the sulfonate group (SO_3^-).[37] The symmetric stretching peak gradually shifted to higher wavenumber with the increase of $CsPbI_3$ content in the solution, indicating the interaction between the sulfonate group and cations in the precursor solution. The increase of S=O stretching wavenumber could be explained by the decreased spatial symmetry of the SO_3^- group after cations bond to certain oxygen elements on the SO_3^- group, and thus the symmetric stretching vibration became harder. Further evidence for the existence of interaction between the zwitterion and metal ions is that the added zwitterion could reduce the size of the colloids in the precursor solution, which was revealed by the Tyndall effect. The Tyndall effect is a light-scattering effect caused by suspended colloids as a light beam passes through a colloidal solution, which makes the light beam visible in the colloidal solution. The amount of scattering depends on the size and density of the colloids. A previous study has reported that $MAPbI_3$ precursor solutions exhibited a strong Tyndall effect, because the solutions contained a large quantity of PbI_2 and lead polyiodide colloids tens to hundreds of nanometers in size.[38] In addition, reducing the colloid size was found to be correlated with reduction in grain size in the $MAPbI_3$ films, because the colloids serve as the building blocks for $MAPbI_3$ perovskite grains.[38] We confirmed that $CsPbI_3$ precursor solution also shown a strong Tyndall effect. As shown in Figure S4, a bright beam path was observed in the $CsPbI_3$ precursor solution, while purified deionized water with no colloid did not show any light path. Then we studied the extent of light scattering in $CsPbI_3$ precursor solutions with or without the zwitterion with UV-visible spectroscopy. UV-visible spectroscopy quantifies the total light that is absorbed, scattered, reflected, and refracted by the sample at each wavelength. When the wavelength range is larger than the bandgap, the sample absorption is negligible and the difference in light scattering between $CsPbI_3$ precursor solutions with or without the zwitterion is revealed. We first prepared and measured the $CsPbI_3$ colloidal solution without zwitterion, which showed an absorption cut-off at ~500 nm and strong light scattering at a wavelength larger than 500 nm (Figure 2E). Then SB3-10 zwitterion powder was gradually added to the original $CsPbI_3$ precursor solution, and the spectrum of the solution was measured. As shown in Figure 2E, light scattering was gradually reduced after adding SB3-10 zwitterion to the precursor solution, indicating the reduction in colloid size by the zwitterion interaction in the colloidal solution.

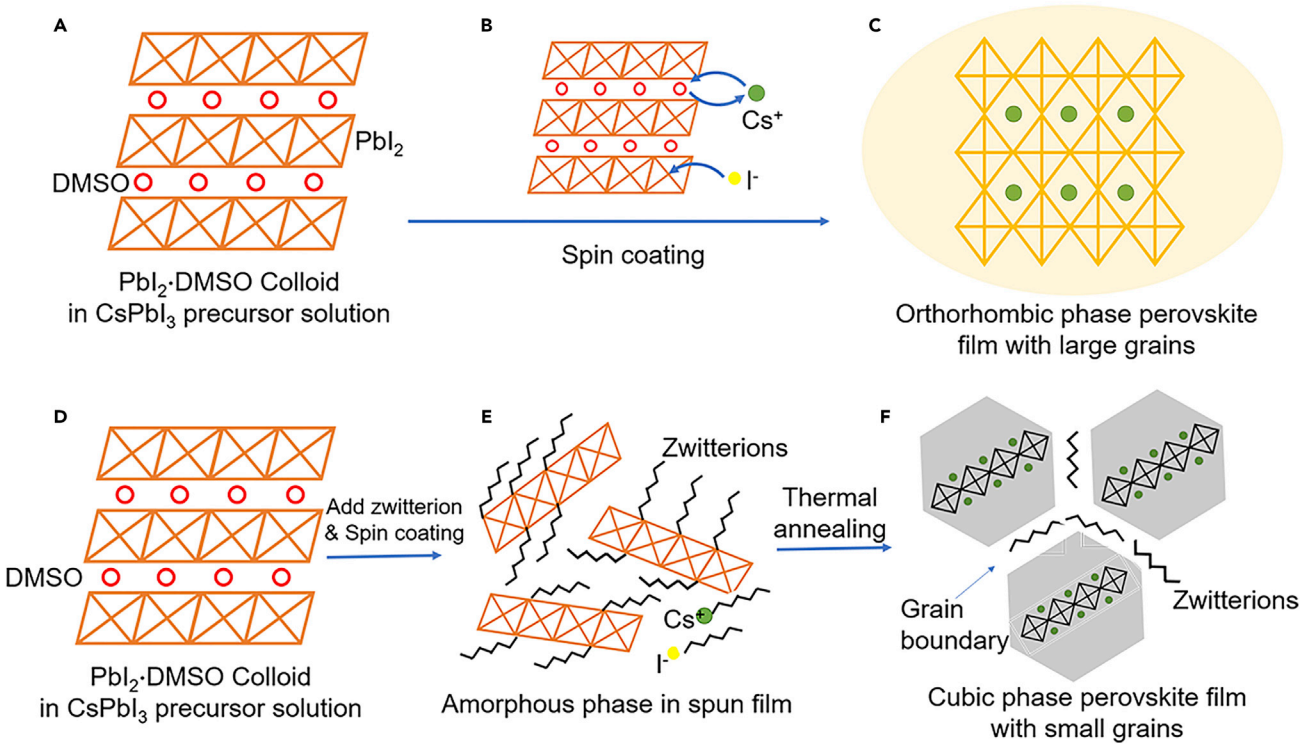

Figure 3. Mechanism of $CsPbI_3$ α-Phase Stabilization by Zwitterion

(A–F) Schematic representation of $CsPbI_3$ crystal formation from precursor solution without (A–C) or with (D–F) the zwitterion. PbI_2 in the precursor solution coordinates with DMSO molecules to form crystallized PbI_2·DMSO colloids (A). Without the zwitterion, I^- ions in the solution facilely coordinate to Pb^{2+} ions of the PbI_2·DMSO colloid to form corner-sharing $[PbI_6]^{4-}$ octahedra, and Cs^+ ions occupy the octahedral sites (B), resulting in large-grained $CsPbI_3$ film with orthorhombic phase (C). With zwitterion, the size of the PbI_2·DMSO colloids (D) is decreased because zwitterions can interact with Cs^+ and I^- ions in the precursor solution (E). The spun film before annealing shows amorphous phase (E). (F) The zwitterion molecules are expelled toward the grain surface and GBs during $CsPbI_3$ grain growth, which maintains the small grains by impeding further grain growth.

Based on the above characterizations and discussion, we show the grain formation processes of $CsPbI_3$ films from precursor solutions with or without the zwitterion in Figures 3A–3F. We speculate that the process of $CsPbI_3$ perovskite formation is similar to that of $MAPbI_3$ formation, both of which involve the formation of $[PbI_6]^{4-}$ octahedra from PbI_2 and octahedral site occupation by cations. Figures 3A–3C shows the steps of $CsPbI_3$ perovskite formation from $CsPbI_3$ precursor solution without zwitterion. As shown in Figure 3A, PbI_2 in the $CsPbI_3$ precursor solution coordinates with DMSO molecules to form crystallized PbI_2·DMSO colloid. During spin coating of the precursor solution, I^- ions in the solution coordinate to Pb^{2+} ions of the PbI_2·DMSO colloid to form corner-sharing $[PbI_6]^{4-}$ octahedra, and Cs^+ ions occupy the octahedral sites to form $CsPbI_3$ perovskite (Figures 3B and 3C). Without zwitterion in the precursor solution, this process occurs quickly at room temperature because of the rapid crystallization of $CsPbI_3$ perovskite, resulting in large $CsPbI_3$ grains with orthorhombic phase. In contrast, with zwitterion in the precursor solution, the electrostatic interaction between zwitterion and PbI_2·DMSO colloids can break the layered structure of the colloids to decrease the colloid size (Figures 3D and 3E). The crystallization of $CsPbI_3$ perovskite is suppressed, resulting in amorphous phase in the spun film before thermal annealing (Figure 3E). During the $CsPbI_3$ grain growth process, the zwitterions molecules are expelled to the grain boundaries (GBs) and grain surface, which may maintain the grain size by impeding further grain growth (Figure 3F).

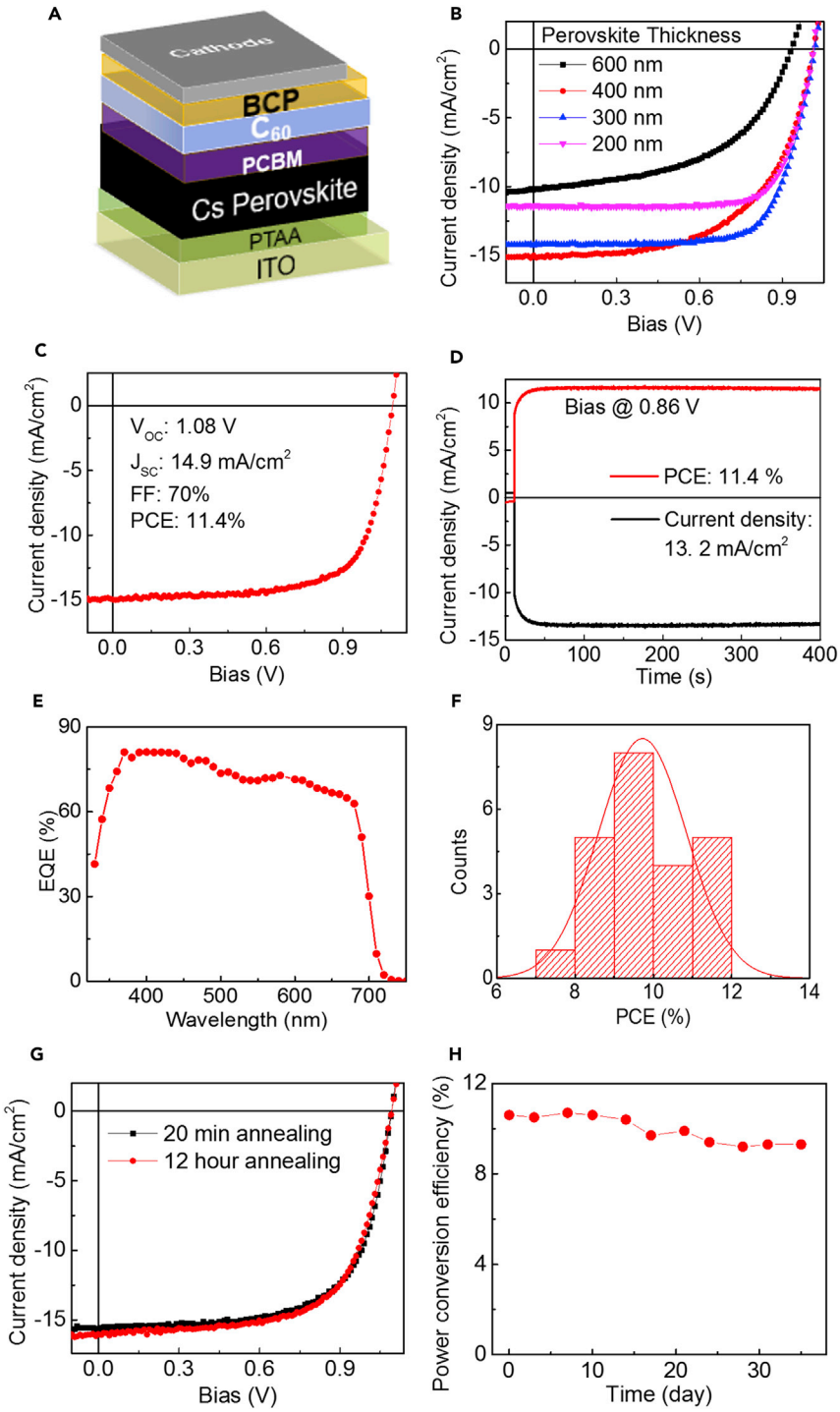

Figure 4. Performance of Cesium Perovskite Solar Cells

(A) Structure of the cesium perovskite solar cells.

(B) *J-V* curves of the devices with cesium perovskite layers of different thicknesses. NDSB201 was used to stabilize perovskite α phase and the perovskite composition was $CsPb(I_{0.98}Cl_{0.02})_3$.

(C) *J-V* curve of the champion $CsPb(I_{0.98}Cl_{0.02})_3$ device with perovskite layer treated by argon plasma. The thickness of the perovskite layer was 300 nm.

(D) Steady-state measurement of the photocurrent and PCE of the most efficient device.

(E) EQE of the most efficient device.

Figure 4. *Continued*

(F) The statistics of PCE distribution for $CsPb(I_{0.98}Cl_{0.02})_3$ devices with argon plasma treatment.

(G) *J-V* curves of $CsPb(I_{0.98}Cl_{0.02})_3$ devices with the perovskite layer annealed at 90°C for 20 min and 12 hr.

(H) PCE of a typical $CsPb(I_{0.98}Cl_{0.02})_3$ device kept in an ambient environment as a function of storage time. The sample was kept in air without encapsulation under dark conditions.

We also considered the possible interaction between zwitterion and perovskite in the zwitterion-$CsPbI_3$ films, which may cause additional surface strain to stabilize the α phase. However, this scenario was excluded, because no strong interaction was found between zwitterion and $CsPbI_3$ in the films after thermal annealing. Figure S5 shows the FTIR spectrum of solid SB3-10 powder and the spectrum of SB3-10-perovskite films. No obvious peak shift was observed for the symmetric S=O stretching vibration modes, which is different from the zwitterion interaction in the precursor solution (Figure 2D). The FTIR peak splitting of the powder SB3-10 sample at ~1,035 cm^{-1} may be caused by the high packing density of zwitterion molecules in the powder sample, which has been observed in a previous study.[37]

Photovoltaic Device Performance of Zwitterion-Stabilized $CsPbI_3$

We further fabricated solar cells to investigate the photovoltaic performance of the zwitterion-stabilized $CsPbI_3$ films. Figure 4A shows the structure of the solar-cell device used in this study. All the solar-cell devices used NDSB201 to stabilize the $CsPbI_3$ α phase, because it exhibited better efficiency as shown in Figure S6. We first optimized the composition of perovskite to increase the efficiency of the device. It was found that precursor composition of $CsPb(I_{0.98}Cl_{0.02})_3$ gave higher efficiency with increased open circuit voltage (V_{OC}) of 1.01 V, compared with 0.85 V for the composition of $CsPbI_3$ (Figure S7). Cl most likely stayed in the annealed films, as the PL peak of the $CsPb(I_{0.95}Cl_{0.05})_3$ film exhibited a blue shift by ~10 nm compared with that of the $CsPbI_3$ film (Figure S8). Figure 4B shows the *J-V* curves of $CsPb(I_{0.98}Cl_{0.02})_3$ perovskite devices with different thicknesses of the perovskite layers. The film thickness was altered by changing the concentration of the precursor solution, and the thickness was measured by a step profiler or cross-section SEM. The device with a 600 nm perovskite layer had a short-circuit current (J_{SC}) of 10.2 mA/cm^2, a V_{OC} of 0.92 V, a fill factor (FF) of 52%, and a PCE of 4.9%. Reducing the perovskite film thickness to 400 nm increased the PCE of the device to 8.8% by enhancing J_{SC} to 15.2 mA/cm^2 and V_{OC} to 1.01 V. The best efficiency was obtained in the devices with a 300 nm perovskite layer, exhibiting a V_{OC} of 1.0 V, a J_{SC} of 14.2 mA/cm^2, FF of 73% and a PCE of 10.4%. Further decreasing the thickness of the perovskite layer to 200 nm significantly reduced light absorption and thus reduced the J_{SC} to 11.5 mA/cm^2.

The increased current in devices with thinner perovskite layers indicates that the photocurrent output is most likely limited by charge carrier extraction, because the grain size of the zwitterion-stabilized films was only ~30 nm. The zwitterion molecules in the GBs of perovskite films may limit charge carrier transport, although they help to stabilize the black phase. Partial removal of the zwitterion molecules after α-phase perovskite film formation may further increase the efficiency of the device. In quantum dot solar cells, washing the quantum dot films with solvent can partially remove unreacted ligands to increase the efficiency of the device.[25,39] The ligand washing process requires selecting a suitable solvent, which is not compatible here, because most polar solvents for dissolving zwitterions could also dissolve cesium perovskite. Encouragingly, we applied another method, argon plasma treatment, to etch the zwitterion molecules on the $CsPb(I_{0.98}Cl_{0.02})_3$ film surface, which turned out to be an effective way to increase the efficiency of the device. Plasma

treatment was expected to remove the zwitterion with little damage to the inorganic perovskite, because organic material generally has a much higher sputtering rate under ion bombardment than inorganic materials. Figure 4C shows the *J-V* curve of the $CsPb(I_{0.98}Cl_{0.02})_3$ device after plasma treatment. A champion device efficiency was obtained, with a V_{OC} of 1.09 V, a J_{SC} of 14.9 mA/cm^2, FF of 70% and a PCE of 11.4%. Figure 4D shows the steady photocurrent and PCE measured at the maximum power output point (0.86 V) of the most efficient device. The steady photocurrent and stabilized PCE measured at the maximum power point agree well with the values from the *J-V* curve. The external quantum efficiency (EQE) of the best device is shown in Figure 4E, which shows an integrated photo current of 14.5 mA/cm^2. The statistics of PCE distribution for $CsPb(I_{0.98}Cl_{0.02})_3$ devices in Figure 4F demonstrate the reliability and the repeatability of the cesium perovskite solar cells. Although significant efficiency enhancement has been demonstrated, the plasma treatment could not remove the zwitterion molecules at the GBs of the perovskite films. Removing zwitterion in GBs or using other zwitterions with higher conductivity may further increase the efficiency of the cesium perovskite device.

Inorganic cesium perovskites showed superior thermal stability compared with those OIHPs with organic cations. We annealed the cesium perovskite films at 90°C overnight and fabricated devices to test the thermal stability of the films. As shown in Figure 4G, the control device with perovskite film annealed at 20 min shows a J_{SC} of 15.6 mA/cm^2, a V_{OC} of 1.08 V, FF of 67%, and a PCE of 11.2%, which represents a typical efficiency of $CsPb(I_{0.98}Cl_{0.02})_3$ devices treated with argon plasma. Interestingly, the devices with the perovskite layer annealed at 90°C for 12 hr showed comparable efficiency of 11.3%. The same experiment was conducted on $MAPbI_3$ devices as a control group. As shown in the Figure S9, a dramatic reduction in efficiency was observed in the $MAPbI_3$ device from 18.2% to 11.3%. In addition, the inorganic cesium perovskite devices also demonstrated good air stability. As shown in Figure 4H, the device maintained ~85% of its original efficiency after storage in air for over 30 days.

Conclusions

In conclusion, we reported a facile process to stabilize α-phase cesium perovskites at room temperature, which enables the fabrication of solution-processed cesium perovskite devices with efficiency over 11%. We elucidated that the sulfobetaine zwitterions could interact with ions and colloids in the $CsPbI_3$ precursor solution, which impeded the crystallization of perovskite to form small-grained $CsPbI_3$ films. These α-phase cesium perovskite materials may find promising applications in other areas such as light-emitting diodes and photodetectors. This study also points out a new direction to control the crystallization of perovskite thin films to manipulate thermodynamic phase stability, which might be further used in stabilizing the black phase of other promising perovskite materials, such as $FAPbI_3$ and $CsSnI_3$.

EXPERIMENTAL PROCEDURES

$CsPbI_3$ Film Fabrication and Characterization

The methods for cleaning indium tin oxide (ITO) glass and Poly[bis(4-phenyl)(2,4,6-trimethylphenyl)amine] (PTAA) film fabrication can be found elsewhere.[40] The $CsPbI_3$ perovskite films were fabricated by a one-step method, where an equal molar ratio of lead iodide (PbI_2) and cesium iodide (CsI) were mixed in DMSO/dimethylformamide (DMF) mixed solvent (v/v, 1/4).[33] Three sulfobetaine zwitterions, 3-(1-pyridinio)-1-propanesulfonate (NDSB201), 3-[2-hydroxyethyl(dimethyl)azaniumyl] propane-1-sulfonate (NDSB211), 3-(decyldimethylammonio) propane-1-sulfonate (SB3-10), were added to the $CsPbI_3$ precursor solution to stabilize the cubic phase

of $CsPbI_3$ films. A typical ratio of zwitterion added in $CsPbI_3$ solution was 1.5% (weight ratio of zwitterion to $CsPbI_3$). The zwitterion materials were purchased from Sigma-Aldrich and used as received. The precursor solutions were spin coated on top of PTAA substrates at a spin speed of 4,000 rpm. Then the films were annealed at 65°C for 5 min, followed by annealing at 90–100°C for 20 min.

XRD of the films was recorded on a BrukerAXS D8 Discover diffractometer. The long-term stability study in Figure 1E was conducted by storing the samples in dark conditions in air. The air humidity during the 60 testing days varied between 17% and 100%, with a typical humidity level of 30%–40%. Diamond software was used to simulate the XRD pattern of cubic-phase $CsPbI_3$. The lattice constant and space group of $CsPbI_3$ was from previous literature.[41] The samples for XRD measurement in Figure 2C were measured immediately after fabrication. No thermal annealing was applied to the samples before measurement. The samples were sealed in bottles in an N_2 glovebox and then transferred from the glovebox to the XRD equipment to minimize the exposure to air.

SEM of the films was recorded on an FEI Helios FIB/SEM 660. The grain size was determined on cross-section SEM images and estimated using Nano Measure software. The grains have an irregular shape. In order to get an accurate size distribution, the size of all the grains was measured in the same lateral direction, and all grains in the SEM images were included in the statistics without selection. The average grain size was derived by fitting the data with Gaussian distribution.

FTIR was characterized using a Spectrum Two FTIR (PerkinElmer) with universal attenuated total reflectance (Single Reflection Diamond). The SB3-10 solution for the FTIR measurements in Figure 2D was prepared by dissolving SB3-10 powder in DMF at 0.1 M concentration. Then 0.5 M $CsPbI_3$ solution (DMF as solvent) was added to the SB3-10 solution to obtain the desired SB3-10/$CsPbI_3$ ratios.

Absorption spectra and photoluminescence (PL) spectra were recorded on an Evolution 201 UV-visible spectrophotometer and iHR320 photoluminescence spectroscopy, respectively. The $CsPbI_3$ precursor solution for UV-visible spectrum measurement in Figure 2E was prepared by dissolving equal molar concentrations (1 M) of CsI and PbI_2 in DMF/DMSO (v/v, 4/1). Then SB3-10 powder was gradually added to the solution to obtain the desired $CsPbI_3$/SB3-10 ratios.

Cesium Perovskite Solar-Cell Fabrication

The fabrication of the device was conducted in a glovebox with the oxygen level lower than 100 particles per million. Details about the preparation of the $CsPbI_3$ perovskite precursor solution can be found above. To increase the wetting property of cesium perovskite precursor on PTAA film, the PTAA-coated ITO substrate was pre-wetted by spinning 50 μL of DMF at 4,000 rpm for 5 s. 90 μL of cesium perovskite precursor was spin coated on PTAA substrate at 2,000 rpm for 2 s followed by 4,000 rpm for 45 s. The sample was drop casted with 90 μL toluene at 15 s after the start of spin coating. $CsPbI_3$ solutions with different concentrations were used to control the thickness of the spun film. $CsPbI_3$ films 200 nm, 300 nm, 400 nm, and 600 nm thick were made with 0.4 M, 0.65 M, 0.8 M, and 1.2 M solutions, respectively. Lead bromide and lead chloride were used to tune the composition of the perovskite precursor solutions to $CsPb(I_{0.98}Br_{0.02})_3$ and $CsPb(I_{0.98}Cl_{0.02})_3$. The spun films were annealed at 90°C for 20 min. The argon plasma treatment was conducted with a PE-50 plasma cleaning system purchased from Plasma Etch. Typically, the cesium perovskite samples were treated at an operating power of 210 W for 2–6 s. Then, 2 wt % [6,6]-phenyl-C61-butyric acid methyl ester (PCBM) dissolved in

dichlorobenzene was spin coated on perovskite layer at 6,000 rpm for 35 s and then annealed at 90°C for 30 min. After deposition of PCBM layers, 25 nm C_{60} was thermally evaporated at a deposition rate of 0.5 Å/s. The devices were finished by the evaporation of 7 nm 2,9-dimethyl-4,7-diphenyl-1,10-phenanthroline (BCP) and 100 nm aluminum or copper electrode. Cooling water was used to cool the samples to room temperature during the deposition of C_{60}, BCP, and electrode. The area of the device was defined as the overlap of ITO with cathode. Slight variation in the area of the device was observed in devices from different batches. Optical microscopy was used to measure the active area accurately; the area typically measured 2.0 × 5.0 mm.

Device Characterization

The *J-V* curves of the devices were measured in a glovebox. AM 1.5G irradiation (100 mW cm^{-2}) with a xenon-lamp-based solar simulator (Oriel 67,005, 150 W Solar Simulator) was used as the light source. A Schott visible-color glass-filtered (KG5 color-filtered) Si diode (Hamamatsu S1133) was used to calibrate the light intensity before photocurrent measurements. A Keithley 2400 Source-Meter was used to record the *J-V* curves. The scanning direction for the *J-V* measurements was from positive bias to negative bias. The voltage scanning rate was 0.05 V s^{-1}. The steady-state photocurrent in Figure 4D was measured by recording the champion device photocurrent under 0.86 V bias. Then the steady-state PCE was obtained by multiplying the measured current by 0.86 V. EQE curves were characterized with a Newport QE measurement kit by focusing a monochromatic beam of light onto the devices.

SUPPLEMENTAL INFORMATION

Supplemental Information includes nine figures and can be found with this article online at http://dx.doi.org/10.1016/j.joule.2017.07.017.

AUTHOR CONTRIBUTIONS

J.H. conceived the idea and supervised the project. Q.W. and X.Z. fabricated the devices and conducted most of the measurements. Y.D. and J.Z. conducted the XRD measurements and analyzed the data. Z.C. conducted the FTIR measurements and analyzed the data. Q.W. and J.H. wrote the paper.

ACKNOWLEDGMENTS

This work is supported by the Department of Energy (DE-EE0006709) and the Office of Naval Research (N00014-15-1-2713).

Received: June 20, 2017
Revised: July 17, 2017
Accepted: July 31, 2017
Published: September 13, 2017

REFERENCES

1. Green, M.A., Ho-Baillie, A., and Snaith, H.J. (2014). The emergence of perovskite solar cells. Nat. Photon. *8*, 506–514.

2. McGehee, M.D. (2014). Perovskite solar cells: continuing to soar. Nat. Mater. *13*, 845–846.

3. Brenner, T.M., Egger, D.A., Kronik, L., Hodes, G., and Cahen, D. (2016). Hybrid organic-inorganic perovskites: low-cost semiconductors with intriguing charge-transport properties. Nat. Rev. Mater. *1*, 15007.

4. Zhang, W., Eperon, G.E., and Snaith, H.J. (2016). Metal halide perovskites for energy applications. Nat. Energy *1*, 16048.

5. Park, N.-G., Grätzel, M., Miyasaka, T., Zhu, K., and Emery, K. (2016). Towards stable and commercially available perovskite solar cells. Nat. Energy *1*, 16152.

6. McMeekin, D.P., Sadoughi, G., Rehman, W., Eperon, G.E., Saliba, M., Hörantner, M.T., Haghighirad, A., Sakai, N., Korte, L., Rech, B., et al. (2016). A mixed-cation lead mixed-halide perovskite absorber for tandem solar cells. Science *351*, 151–155.

7. Saliba, M., Matsui, T., Domanski, K., Seo, J., Ummadisingu, A., Zakeeruddin, S.M., Correa-Baena, J., Tress, W.R., Abate, A., Hagfeldt, A.,

et al. (2016). Incorporation of rubidium cations into perovskite solar cells improves photovoltaic performance. Science *354*, 206–209.

8. Yang, W.S., Noh, J., Jeon, N., Kim, Y., Ryu, S., Seo, J., and Seok, S. (2015). High-performance photovoltaic perovskite layers fabricated through intramolecular exchange. Science *348*, 1234–1237.

9. Zhou, H., Chen, Q., Li, G., Luo, S., Song, T., Duan, H., Hong, Z., You, J., Liu, Y., and Yang, Y. (2014). Interface engineering of highly efficient perovskite solar cells. Science *345*, 542–546.

10. Eperon, G.E., Leijtens, T., Bush, K.A., Prasanna, R., Green, T., Wang, J., McMeekin, D.P., Volonakis, G., Milot, R.L., May, R., et al. (2016). Perovskite-perovskite tandem photovoltaics with optimized band gaps. Science *354*, 861–865.

11. Tan, H., Jain, A., Voznyy, O., Lan, X., Pelayo García de Arquer, F., Fan, J.Z., Quintero-Bermudez, R., Yuan, M., Zhang, B., Zhao, Y., et al. (2017). Efficient and stable solution-processed planar perovskite solar cells via contact passivation. Science *355*, 722–726.

12. Zhao, D., Yu, Y., Wang, C., Liao, W., Shrestha, N., Grice, C.R., Cimaroli, A.J., Guan, L., Ellingson, R.J., Zhu, K., et al. (2017). Low-bandgap mixed tin–lead iodide perovskite absorbers with long carrier lifetimes for all-perovskite tandem solar cells. Nat. Energy *2*, 17018.

13. Yang, M., Li, Z., Reese, M.O., Reid, O.G., Kim, D., Siol, S., Klein, T.R., Yan, Y., Berry, J.J., van Hest, M., et al. (2017). Perovskite ink with wide processing window for scalable high-efficiency solar cells. Nat. Energy *2*, 17038.

14. Bush, K.A., Palmstrom, A.F., Yu, Z., Boccard, M., Cheacharoen, R., Mailoa, J.P., McMeekin, D.P., Hoye, R.L.Z., Bailie, C.D., Leijtens, T., et al. (2017). 23.6%-efficient monolithic perovskite/silicon tandem solar cells with improved stability. Nat. Energy *2*, 17009.

15. National Renewable Energy Laboratory. Photovoltaic research. http://www.nrel.gov/ncpv/images/efficiency_chart.jpg.

16. Conings, B., Drijkoningen, J., Gauquelin, N., Babayigit, A., D'Haen, J., D'Olieslaeger, L., Ethirajan, A., Verbeeck, J., Manca, J., and Mosconi, E. (2015). Intrinsic thermal instability of methylammonium lead trihalide perovskite. Adv. Energy Mater. *5*, 1500477.

17. Nagabhushana, G., Shivaramaiah, R., and Navrotsky, A. (2016). Direct calorimetric verification of thermodynamic instability of lead halide hybrid perovskites. Proc. Natl. Acad. Sci. USA *113*, 7717–7721.

18. Sutton, R.J., Eperon, G.E., Miranda, L., Parrott, E.S., Kamino, B.A., Patel, J.B., Hörantner, M.T., Johnston, M.B., Haghighirad, A.A., and Moore, D.T. (2016). Bandgap-tunable cesium lead halide perovskites with high thermal stability for efficient solar cells. Adv. Energy Mater. *6*, 1502458.

19. Beal, R.E., Slotcavage, D.J., Leijtens, T., Bowring, A.R., Belisle, R.A., Nguyen, W.H., Burkhard, G.F., Hoke, E.T., and McGehee, M.D. (2016). Cesium lead halide perovskites with improved stability for tandem solar cells. J. Phys. Chem. Lett. *7*, 746–751.

20. Sharma, S., Weiden, N., and Weiss, A. (1992). Phase diagrams of quasibinary systems of the type: ABX3—a′ BX3; ABX3—AB′ X3, and ABX3—ABX′ 3; X= Halogen. Z. Phys. Chem. *175*, 63–80.

21. Stoumpos, C.C., Malliakas, C.D., and Kanatzidis, M.G. (2013). Semiconducting tin and lead iodide perovskites with organic cations: phase transitions, high mobilities, and near-infrared photoluminescent properties. Inorg. Chem. *52*, 9019–9038.

22. Chen, C.Y., Lin, H.Y., Chiang, K.M., Tsai, W.L., Huang, Y.C., Tsao, C.S., and Lin, H.W. (2017). All-vacuum-deposited stoichiometrically balanced inorganic cesium lead halide perovskite solar cells with stabilized efficiency exceeding 11%. Adv. Mater. *29*, 1605290.

23. Ma, Q., Huang, S., Wen, X., Green, M.A., and Ho-Baillie, A.W. (2016). Hole transport layer free inorganic $CsPbIBr_2$ perovskite solar cell by dual source thermal evaporation. Adv. Energy Mater. *6*, 1502202.

24. Frolova, L.A., Anokhin, D.V., Piryazev, A.A., Luchkin, S.Y., Dremova, N.N., Stevenson, K.J., and Troshin, P.A. (2016). Highly efficient all-inorganic planar heterojunction perovskite solar cells produced by thermal coevaporation of CsI and PbI_2. J. Phys. Chem. Lett. *8*, 67–72.

25. Swarnkar, A., Marshall, A.R., Sanehira, E.M., Chernomordik, B.D., Moore, D.T., Christians, J.A., Chakrabarti, T., and Luther, J.M. (2016). Quantum dot–induced phase stabilization of α-$CsPbI_3$ perovskite for high-efficiency photovoltaics. Science *354*, 92–95.

26. McHale, J., Auroux, A., Perrotta, A., and Navrotsky, A. (1997). Surface energies and thermodynamic phase stability in nanocrystalline aluminas. Science *277*, 788–791.

27. Frey, M., and Payne, D. (1996). Grain-size effect on structure and phase transformations for barium titanate. Phys. Rev. B *54*, 3158.

28. Fu, D., Suzuki, H., and Ishikawa, K. (2000). Size-induced phase transition in $PbTiO_3$ nanocrystals: Raman scattering study. Phys. Rev. B *62*, 3125.

29. Zhang, N., Yang, W., Ding, W., Xing, D., and Du, Y. (1999). Grain size-dependent magnetism in fine particle perovskite, $La_{1-x}Sr_xMnO_z$. Solid State Commun. *109*, 537–542.

30. Ayyub, P., Palkar, V., Chattopadhyay, S., and Multani, M. (1995). Effect of crystal size reduction on lattice symmetry and cooperative properties. Phys. Rev. B *51*, 6135.

31. Jeon, N.J., Noh, J.H., Kim, Y.C., Yang, W.S., Ryu, S., and Seok, S.I. (2014). Solvent engineering for high-performance inorganic–organic hybrid perovskite solar cells. Nat. Mater. *13*, 897–903.

32. Xiao, M., Huang, F., Huang, W., Dkhissi, Y., Zhu, Y., Etheridge, J., Gray-Weale, A., Bach, U., Cheng, Y.B., and Spiccia, L. (2014). A fast deposition-crystallization procedure for highly efficient lead iodide perovskite thin-film solar cells. Angew. Chem. *126*, 10056–10061.

33. Chen, B., Bai, Y., Yu, Z., Li, T., Zheng, X., Dong, Q., Shen, L., Boccard, M., Gruverman, A., and Holman, Z. (2016). Efficient semitransparent perovskite solar cells for 23.0%-efficiency perovskite/silicon four-terminal tandem cells. Adv. Energy Mater. *6*, 1601128.

34. Protesescu, L., Yakunin, S., Bodnarchuk, M.I., Krieg, F., Caputo, R., Hendon, C.H., Yang, R.X., Walsh, A., and Kovalenko, M.V. (2015). Nanocrystals of cesium lead halide perovskites ($CsPbX_3$, X= Cl, Br, and I): novel optoelectronic materials showing bright emission with wide color gamut. Nano Lett. *15*, 3692–3696.

35. Hoffman, J.B., Schleper, A.L., and Kamat, P.V. (2016). Transformation of sintered $CsPbBr_3$ nanocrystals to cubic $CsPbI_3$ and gradient $CsPbBr_xI_{3-x}$ through halide exchange. J. Am. Chem. Soc. *138*, 8603–8611.

36. Wang, C., Chesman, A.S., and Jasieniak, J.J. (2017). Stabilizing the cubic perovskite phase of $CsPbI_3$ nanocrystals by using an alkyl phosphinic acid. Chem. Commun. *53*, 232–235.

37. Viana, R.B., da Silva, A.B., and Pimentel, A.S. (2012). Infrared spectroscopy of anionic, cationic, and zwitterionic surfactants. Adv. Phys. Chem. *2012*, 903272.

38. Yan, K., Long, M., Zhang, T., Wei, Z., Chen, H., Yang, S., and Xu, J. (2015). Hybrid halide perovskite solar cell precursors: colloidal chemistry and coordination engineering behind device processing for high efficiency. J. Am. Chem. Soc. *137*, 4460–4468.

39. Wang, R., Shang, Y., Kanjanaboos, P., Zhou, W., Ning, Z., and Sargent, E.H. (2016). Colloidal quantum dot ligand engineering for high performance solar cells. Energy Environ. Sci. *9*, 1130–1143.

40. Wang, Q., Dong, Q., Li, T., Gruverman, A., and Huang, J. (2016). Thin insulating tunneling contacts for efficient and water-resistant perovskite solar cells. Adv. Mater. *28*, 6734–6739.

41. Trots, D., and Myagkota, S. (2008). High-temperature structural evolution of caesium and rubidium triiodoplumbates. J. Phys. Chem. Sol. *69*, 2520–2526.